# Kinematics of an Alpine rock glacier from multi-temporal UAV surveys and GNSS data

Francesca Bearzot [a, *], Roberto Garzonio [a], Biagio Di Mauro [b], Roberto Colombo [a], Edoardo Cremonese [c], Giovanni B. Crosta [a], Reynald Delaloye [d], Christian Hauck [d], Umberto Morra Di Cella [c], Paolo Pogliotti [c], Paolo Frattini [a], Micol Rossini [a]

[a] Department of Earth and Environmental Sciences (DISAT), University of Milano-Bicocca, Piazza della Scienza 1, 20126 Milan, Italy; *f.bearzot@campus.unimib.it; roberto.garzonio@unimib.it; giovannibattista.crosta@unimib.it; roberto.colombo@unimib.it; paolo.frattini@unimib.it; micol.rossini@unimib.it*

[b] Institute of Polar Sciences, National Research Council, Venice, Italy; *biagio.dimauro@cnr.it*

[c] Climate Change Unit, Environmental Protection Agency of Valle d'Aosta, Italy; *e.cremonese@arpa.vda.it; p.pogliotti@arpa.vda.it; u.morradicella@arpa.vda.it*

[d] Department of Geosciences, University of Fribourg, Switzerland; *christian.hauck@unifr.ch; reynald.delaloye@unifr.ch*

## Abstract

The quantification of rock glacier dynamics has gained increasing importance in recent years. In this study, the spatial and temporal flow patterns of perennially frozen debris in the active Gran Sometta rock glacier (Western Italian Alps) were investigated with repeated Unmanned Aerial Vehicle (UAV) surveys (2015-2019), Global Navigation Satellite Systems (GNSS) campaigns (2012-2020), geophysical prospections (2015) and ground surface temperature data (2014-2020).

UAV data were used to generate maps of changes and elevation differences of the rock glacier surface by 3D point cloud comparison to evaluate surface lowering and accumulation processes. Horizontal velocities were quantified by manually selecting clearly identifiable features on the orthomosaics and by an automatic image correlation technique. Results were compared with horizontal surface velocities from GNSS measurements on selected points. The comparison between the manual and automatic computation of horizontal surface velocities against GNSS measurements shows that the highest accuracy was obtain using the image correlation feature-tracking algorithm with an $R^2$ = 0.99 and a RMSE lower than 0.07 m.

Point cloud comparisons show surface lowering in the orographic left hand side of the terminal part and in the central body of the rock glacier. The upper part exhibits almost absence of subsidence and any movement. This is explained by the lack of permafrost in this sector due to its overriding by the development of a small glacier during the Little Ice Age. As a result of the downslope movement, zones of surface rising occurred at the advancing front and at the moving ridge and furrow complexes. Surface velocity decreases from the orographic left to the right hand side of the rock glacier tongue, where a thaw subsidence of up to 0.05 m/y was also observed. According to the GNSS measurements, the range of flow velocity of the rock glacier increased from 0.17-1.1 m/y in 2013 to 0.21-1.45 m/y in 2015 and then decreased until 2018 when the smallest surface velocity is detected. Since 2018, the creep velocities gradually started to increase again reaching values of 0.23 m/y up to a maximum of 1.9 m/y in the orographic left hand side of the rock glacier tongue. This agrees with observations from other rock glaciers in the European Alps in recent decades.

The complex Gran Sometta rock glacier dynamics can be explained by the heterogeneous distribution of permafrost and related subsurface perennially frozen ground which is thick enough (about 20-30 metres) for permafrost creep to occur. Creep rates of the rock glacier permafrost depends also on the ground thermal regime: annual warmer surface conditions promote acceleration phase of creep within the rock glacier permafrost, whereas ground surface cooling causes a slight deceleration of creep rates.

**Keywords:** rock glacier, permafrost creep, UAV, GNSS, point clouds, thermal effects

## 1. Introduction

Active rock glaciers are widely recognized as creep phenomena of mountain permafrost (Haeberli et al., 2006; Barsch, 1992; Wahrhaftig and Cox, 1959). They consist of a mixture of rock/debris and ice, and represent key features to understand the response of mountain cryosphere to climate change (Haeberli and Beniston, 1998).

Changing climatic conditions and in particular the increase of air temperature strongly influence the thermal state of permafrost (Etzelmüller et al., 2020; Biskaborn et al., 2019). Recent studies showed that ground temperature, together with the rock glacier external (i.e. topographical conditions) and internal (i.e. internal structure and composition) characteristics, controls the deformation of perennially frozen ground and the associated rock glacier flow velocities (Haberkorn et al., 2021). In particular, annual variations in rock glacier surface velocities have been related to ground surface temperature (GST) variations that reflect, with a delay of several months, the variations of the temperature of the upper permafrost layers due to the slow propagation of annual surface thermal anomalies deeper into the permafrost layers up to 10-30 m depth (Staub et al., 2016; Delaloye et al., 2010).

During the last decades flow velocities were measured on many rock glaciers in the Alps (Bodin et al., 2018; Kellerer-Pirklbauer et al., 2017; Delaloye et al., 2010; Delaloye et al., 2008). Monitoring changes of rock glacier surface velocity and geometry may provide insights on ongoing processes such as ice melt at the permafrost table or base, deformation of the permafrost body and displacement at shear horizons where 50-95% of the total deformation occurs (Cicoira et al., 2020; Kenner et al., 2019; Cicoira et al., 2019; Delaloye et al., 2010). The rock glacier movement can span from few centimetres to several metres per year, depending on creep characteristics, such as the occurrence and depth of shear horizon, influence of liquid water (Cicoira et al., 2019; Ikeda et al., 2008), topographical factors (e.g. slope angle) (Cicoira et al., 2020; Marcer et al., 2019; Delaloye et al., 2013) and ground thermal regime (Staub et al., 2016; Buchli et al., 2013).

Rock glacier surface geometry changes over time were quantified using tachymetric surveying techniques and differential GPS. More recently, the detection and evaluation of three-dimensional deformations, the generation of velocity fields and the high-resolution reconstruction of rock glacier surface have been made possible by remote sensing techniques (i.e. Unmanned Aerial Vehicle –UAV- surveys, terrestrial and airborne laser scanning and the availability of high-resolution optical remote sensing data) combined with computer-based data processing (Kaufmann et al., 2018; Kummert and Delaloye, 2018; Bauer and Paar, 2003). Structure-from-Motion (SfM) photogrammetry represents a powerful tool for geomorphological research (Hendrickx et al., 2019; James et al., 2019; Westoby et al., 2012) allowing the creation of high-density point clouds, high-resolution orthophoto mosaics and Digital Surface Models (DSMs) starting from extensive datasets of overlapping images.

Digital image correlation of multi-temporal UAV images recently allowed for the quantification of deformation and displacement fields over several landforms, including glaciers, landslides, and rock glaciers (Fey and Krainer, 2020; Rossini et al. 2018; Dall'Asta et al., 2017; Wigmore et al., 2017; Lucieer et al., 2014). Other authors suggested the use of a 3D approach to detect multi-directional surface changes in high mountain areas with complex topography (Zahs et al., 2019; Fey et al., 2015; Kaufmann and Ladstädter, 2003).

In this study, the morphological and dynamic changes of the Gran Sometta rock glacier (south-western Italian Alps, Cervinia, Valle d'Aosta) are analysed and the rock glacier response to climate warming is discussed. This rock glacier was already studied by Dall'Asta et al. (2017) between 2012 and 2015. The estimation of the rock glacier surface displacements was determined by manually identification of corresponding features on the orthophotos and by two automatic procedures applied to both orthophotos and DSMs. In this work, in addition to surface displacement assessment several other aspects were considered such as the internal structure, surface morphology and GST data. Multi-temporal high-resolution UAV surveys were performed from 2015 to 2019 and two Electrical Resistivity Tomography (ERT) profiles were performed to identify the internal structure and potential frozen ground inside the main body of the rock glacier in 2015. In addition to UAV surveys, GNSS campaigns were performed from 2012 to 2020. This paper aims (i) to analyse the 3D surface variations and displacement velocities of the rock glacier and their variability between 2012 and 2020, (ii) to validate the movement rate obtained by manual tracking on the orthophotos and by a feature-tracking algorithm against repeated GNSS measurements and (iii) to understand how the extent of frozen ground at depth across longitudinal ERT profiles affects the horizontal surface velocity.

## 2. Study area

### 2.1 Gran Sometta rock glacier

The study area is located on the south-western side of the central Alps at the head of the Valtournenche Valley (AO, Italy) (Figure 1a). Two lobes, at an elevation ranging from 2630 to 2770 m a.s.l, compose the main body of the rock glacier. It is approximately 400 m long, between 150 and 300 m wide with an apparent thickness of 20-30 m (estimated from the height of rock glacier front). On the orographic left hand side of the main body of the rock glacier tongue, a third lobe (Figure 1c), 215 m wide and 192 m long, has a front located at about 2700 m a.s.l.

The surface of the rock glacier appears as a debris mass consisting of pebbles and angular blocks, in most places lacking any finer-grained matrix. The body is characterized by longitudinal ridges in the extensive central part and a complex of transverse ridges and furrows in the compressive terminal part of the tongue. The debris originates from the rock walls of the Gran Sometta peak, mainly composed by green schists with prasinites, with bands of dolomite and marbles. Soil is absent or only very thin and the matrix is clearly subordinate and sandy-gravelly in nature (Dall'Asta et al., 2017).

The study of morphological and dynamic changes was conducted on four main sectors of the rock glacier body (i.e. external lobe, black lobe, white lobe, and upper part, Figure 1c) based on (i) geomorphological characteristics, (ii) debris cover layer and (iii) previous information on the spatial distribution of displacements (Dall'Asta et al., 2017).

The external lobe (sector I) extends from about 2700 m a.s.l. (front lobe) up to approximately 2750 m a.s.l. The black lobe (sector II) reaches from the ski slope at 2630 m a.s.l. to 2750 m a.s.l., while the white lobe (sector III) ranges in elevation from 2630 to 2715 m a.s.l. The upstream part (sector IV), with elevation ranging from 2715 to 2750 m a.s.l., was the part affected by the LIA glacier and does not show any relevant movement. In the orographic upper left part of the main tongue, a push-moraine developed whose current deformation mode is partly a back-creeping process towards the thalweg where the small LIA glacier tongue was developing. This is creating most of the elongated features visible in this part of the rock glacier.

Although there is a rock glacier landform according to the definition by the IPA Action Group Rock glacier inventories and kinematics (IPA, 2020), the Gran Sometta must be classified as "glacier forefield-connected" (interaction glacier-rock glacier is pervasive but limited to a glacier advance phases such as in the LIA) as reported by the same document. However, throughout the text, the Gran Sometta is simply referred to as "rock glacier".

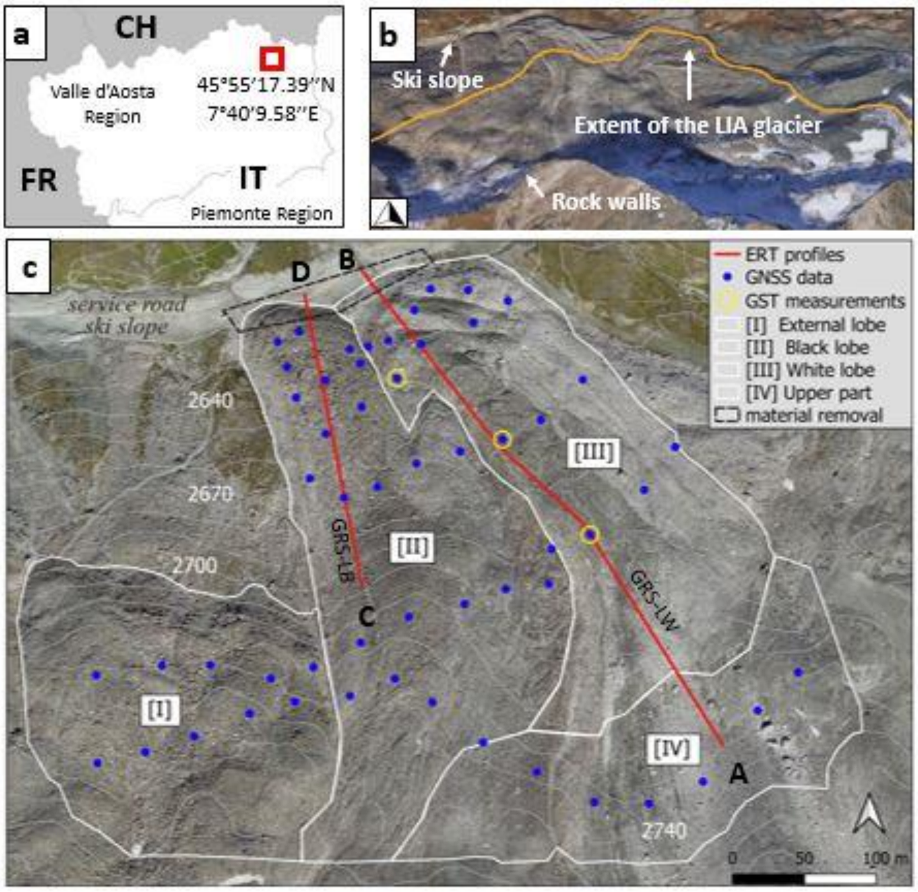


Figure 1. Overview map of the study site. (a) Location of the study site in NW eastern Italian Alps. The coordinates of the rock glacier site are given in the WGS 84 coordinate system; (b) approximate extent of the LIA glacier at Gran Sometta; (c) detail view of the rock glacier with sectors subdivision, locations of the ERT profiles, GNSS measurement points, GST measurements, and artificial reworked area. The orthophoto was taken on August 2016.

## 2.2 Little Ice Age in the Alps and in the Cervinia basin

During the Little Ice Age (LIA, $15^{th}$ – $19^{th}$ century), small glaciers (< 1 $km^2$) were situated over the Alpine permafrost area. Glacier advancements later led to changes in the landscape, visible today with distinct moraine structures (Kneisel and Kääb, 2007; Reynard et al., 2003). The areas temporarily covered by the ice masses were thermally isolated and possibly warmed up while the conditions for perennially frozen sediments and ground ice preservation and formation were favoured at the front and outside these small glaciers, typically on push-moraines (Delaloye and Lambiel, 2008). Push-moraines are glaciotectonized frozen sediments, evidence of geometrical deformation due to glacier dynamics, and represent the morphological expression of permafrost deformation (Reynard et al., 2003; Bennet, 2001; Haeberli, 1979). The retreat of these small glaciers in favourable permafrost conditions has uncovered forefields, some of which containing thick coarse deposits of glacial and periglacial origin, where permafrost can aggrade and/or creep occur. Commonly, the central part of most LIA Alpine glacier forefields is today either permafrost-free or occupied by degrading debris-covered glaciers or buried ice patches (Delaloye and Lambiel, 2008).

The extent of the LIA glacier at Gran Sometta is shown in figure 1b and can only be approximated because there was neither any terminal moraine deposit (common for cold margins of such small glaciers pasting on formerly frozen debris) or because of debris reworking (principally by creep processes). This approximate extent represents the area where geomorphological evidences (e.g. push-moraines and fluted moraines, ground surface texture, absence of debris sorting, bedrock outcrops and surface morphology smoothness) of a glacier extent are visible both on site and remotely.

## 3. Materials and methods

### 3.1 Multi-temporal UAV data

Five UAV surveys of the rock glacier body were conducted from 2015 to 2019 in the absence of snow cover.

The flights of the first and second campaigns were conducted by a senseFly eBee RTK fixed-wing equipped with a SONY DSC-WX220 digital camera (RGB), 4896×3264 pixels resolution and optical sensor size 1/2,3". Missions were planned by using senseFly Emotion 3. Photos were shot from 130 m (and 140 m) above ground level, at a 10-12 m $s^{-1}$ mean flight speed and with 60% and 70% of longitudinal and lateral overlap, respectively. The subsequent surveys were carried out with two different DJI Phantom 4 multicopters: a Phantom 4 Pro (on 2017 and 2018) and a Phantom 4 RTK (on 2019). The first one carries a DJI FC6310 camera with an 8.8 mm nominal focal length, and a 1” CMOS 20-megapixel sensor with 2.41 x 2.41 μm nominal pixel size. The resolution is 5472 x 3648 pixels corresponding to 13.2 x 8.8 mm. The RTK version is equipped with a DJI FC6310R camera which has a glass lens rather than the plastic one fitted on the Phantom 4 Pro. Drone Harmony and DJI GS were used to plan and execute missions.

Further details about the UAV campaigns are reported in Table 1.

| Date | Coverage area (km$^2$) | Ground resolution (cm/px) | Flying altitude (m above ground level) | Camera model | UAV | Number of images |
|---|---|---|---|---|---|---|
| **28/08/2015** | 0.774 | 3.7 | 130 | Sony DSC-WX220 (18,2 Mpx) | senseFly eBee RTK | 280 |
| **24/08/2016** | 0.553 | 4.0 | 140 | Sony DSC-WX220 (18,2 Mpx) | senseFly eBee RTK | 169 |
| **26/08/2017** | 0.407 | 1.8 | 70 | FC6310 | DJI Phantom 4 Pro | 993 |
| **23/08/2018** | 0.418 | 2.4 | 90 | FC6310 | DJI Phantom 4 Pro | 632 |
| **21/08/2019** | 0.366 | 2.1 | 80 | FC6310R | DJI Phantom 4 RTK | 392 |

Table 1. Details of the five UAV surveys performed between 2015 until 2019.

### 3.2 Ground Control Points and GNSS data

Twenty-one photogrammetric markers have been located on the whole study area and their coordinates were measured during drone acquisitions by RTK (Real Time Kinematic) differential GNSS receivers GEOMAX Zenith 20 and Zenith 35 Pro. The position of the markers was determined using a fixed GNSS/RTK base station placed on known position in front of the rock glacier. According to GNSS measurements, the average accuracy of the topographic surveys was 1.8 cm for planimetric coordinates and 2.0 cm for elevation. Approximately 60% of the Ground Control Points (GCPs) were used for orthophoto and DSM generation and the remaining 40% (Check Points – CPs) was used for the validation of the generated models.

The monitoring activity also includes GNSS campaigns. For the black and white lobes, the time series run annually from 2012 to 2020, whereas for the external lobe data acquisition covers the years 2015-2020. GNSS provides highly accurate surface displacement measurements but limited to a few selected points. Here, 54 points (Figure 1c) were used to extract annual surface velocity of the rock glacier and used for the validation of the results derived from photogrammetry. The control points were measured with a GNSS receiver Leica Viva GS10/15 in RTK mode, with an expected precision of 1 cm horizontally and 2 cm in elevation.

### 3.3 Geophysical surveys

On 22 and 23 July 2015, two ERT profiles were performed to characterize the internal structure and identify potential frozen ground inside the main body of the rock glacier. The two profiles were conducted along the flow line direction of the black and white lobes, respectively (see Figure 1c). For both profiles, the Wenner-Schlumberger configuration was adopted. The profile on the white lobe (GRS-LW) was 470 m long with 48 electrodes at 10 m spacing, whereas the profile on the black lobe (GRS-LB) consisted of 48 electrodes with 5 m spacing resulting in 235 m profile length. The measured apparent resistivity data sets were filtered according to Mollaret et al. (2019) and inverted to give the 2-dimensional distribution of specific resistivity using the inversion software Resdinv (Loke, 2020).

### 3.4 Ground surface temperature and meteorological data

Ground surface temperature (GST) is the surface or near-surface temperature of the ground, measured within the uppermost centimetres of it (PermaNET, 2011), and corresponds to the temperature at the top of the active layer. GST measurements were recorded every two hours using autonomous miniature temperature data loggers (MTD's) from 2014 to 2020. Three MTD's are placed on the rock glacier surface (Figure 1c) to monitor the GST in the near sub-surface at depths of one to 10 centimetres, in order to avoid direct radiation influence. Based on the GST measurements, we calculated the mean annual ground surface temperature (MAGST), the ground freezing index (GFI), the ground thawing index (GTI) and the winter equilibrium temperature, WEqT. The MAGST represents a "thermal memory" of the ground of 12-month running mean from August to August and allows identifying periods of cooling or warming of the ground surface. The GFI (and GTI) index is the sum of all daily mean values < 0°C (>0°C) considering the period November-May (June-October) and indicates how cold (or warm) a year was at the ground surface. The WEqT is assessed through the bottom temperature of the winter snow cover (BTS), which measures the temperature at the snow-ground interface (PermaNET, 2011). Therefore, the WEqT is strongly dependent on the snow cover condition (height and duration) and is a valuable indicator of permafrost occurrence. WEqT is the equilibrium value, as a function of the heat flux coming up from the ground, which is reached when the GST stabilises following a sufficient snow cover for insulation from atmospheric variations (PermaNET, 2011).

Additionally, gridded data of air temperature ($T_{air}$) and Snow Water Equivalent (SWE) were generated by the hydrological model GEOtop (Endrizzi et al., 2014) for the study area and solves the energy balance at single grid level (50 m resolution) at hourly step, starting from spatialized meteorological data. $T_{air}$ refers to the daily mean temperature calculated on the rock glacier polygon and by selecting the period from the maximum yearly SWE to the end of the snow season we identified the snowmelt period.

### 3.5 Digital Surface Models, orthophotos generation and point cloud comparison

The Structure from Motion (SfM) technique (Westoby et al., 2012) was used to generate the orthophotos and DSMs using the commercial software Agisoft Metashape, v. 1.5.5. The first step of processing was the selection of images with enough quality and overlap. These photographs were aligned using an image feature recognition algorithm to produce a sparse 3D point cloud by matching coincident features. Secondly, GCPs were manually identified in each photograph and edited when required to georeference the sparse cloud. The coordinates of the GCPs were imported to optimize the spatial accuracy of the 3D point cloud. Thirdly, a multi-view stereo image-matching algorithm was applied to increase the density of the sparse point cloud and to convert it into DSMs and orthomosaics by interpolation. The final products were extracted with a resolution of 5 cm/px. The accuracy of the DSMs and the orthophotos was estimated computing the Root Mean Square Error (RMSE) of the CPs. Successively, we estimated a three-dimensional change of the surface displacements of the rock glacier comparing pairs of point clouds. Overall, we made four models that simulate the surface changes over time. Following Zahs et al. (2019), we quantified changes between each available dataset and the most recent one, for year 2019. The algorithm used was the Multiscale Model to Model Cloud Comparison (M3C2 plug-in) implemented in the open-source software CloudCompare (version v2.11 alpha). M3C2 operates directly on point clouds, computes the local distance between two point clouds along the normal surface direction, which tracks 3D variations in surface orientation. In addition, it estimates for each distance measurement a confidence interval depending on point cloud roughness and registration error (Lague et al., 2013). In our case, the reference cloud is the last cloud acquired in order of time, and the compared cloud changes according to the time interval considered. All clouds were subsampled at 0.05 m minimum point spacing for definition of the core points. The normal and projection scale were selected considering the surface roughness and the point cloud density and change for each compared dataset. The multi-scale estimation was applied into the normal scale parameter in which the minimum normal scale should be at least 20 times higher than the surface roughness at this scale, based on recommendations given in Lague et al. (2013). The projection scale was set to 1, for the 2018-2019 and 2017-2019 comparisons, and to 1.5 for the 2016-2019 and 2015-2019 intervals. The maximum depth was set at 12 m since we do not expect that magnitude of the surface change can exceed this threshold for any time interval. We used the CP RMSE of the different surveys to compute the registration error (*reg*) of the clouds by the following formula:

$$reg = \sqrt{(RMSE_x)^2 + (RMSE_{2019})^2} \quad (1)$$

where the x indicates the year used for the comparison with the year 2019.

The *reg* is assumed isotropic and spatially uniform. Using the *reg* and considering the local point cloud roughness $\sigma_1(d)$ and $\sigma_2(d)$ measured along the normal directions, we calculated the $LOD_{95\%}$ (Level of Detection at 95%) as:

$$LOD_{95\%} = \pm 1.96\left(\sqrt{((\sigma_1(d)^2/n_1)) + ((\sigma_2(d)^2/n_2))} + reg\right) \quad (2)$$

where $n_1$ and $n_2$ are the point clouds. Surface changes are considered statistically significant when exceeding the $LOD_{95\%}$ value (Lague et al. 2013).

The M3C2 plug-in generates a *distance map* that provides an accurate orthogonal distance measurement between two point clouds. From the output table of the M3C2 distance values, the empirical cumulative distribution function (ECDF) was plotted for the annual estimates of the rock glacier surface changes. In addition, the plug-in generates several other products such as the *change significant map* (indicates whether the distance probably correspond to a real change or not) and the *xyz component* of the local surface normal vectors. The predominance of one of these components, horizontal or vertical, indicates the preferential orientation of the surface changes (Lague et al.,2013).

The horizontal ground displacements and the velocity rates of the rock glacier were computed through manual identification, performed by a trained operator, of well recognizable corresponding features (boulders, stones etc.) in two subsequent acquisitions as in Dall'Asta et al. (2017). The feature selection was carried out (i) considering the orientation of the selected feature (i.e. block) and avoiding any rotation that may influence the displacement measurement and (ii) at constant scale so that the chosen point (pixel) was recognised with the same detail over the years. Furthermore, the displacement vectors were also estimated using the feature-tracking algorithm IMCORR (Fey and Krainer, 2020; Vivero and Lambiel, 2019; Fey et al., 2015), implemented in the SAGA GIS open source software (v. 2.3.2). The correlation process is based on finding similar features in two images acquired on the same area at different times. The estimation of the displacement vectors is based on the chosen size of the search window, identified in the least recent image, and searched it in the most recent one. The vector between the centre of the search window of the first image and the peak of the maximum correlation in the second image defines length and direction of displacement features (Fahnestock et al., 1992). Having very variable displacement values, ranging from 0.1 to 2.0 m/y, several interactions of the algorithm were computed to obtain a set of coherent vector fields. This was achieved by varying the dimensions of the search and the reference sizes, imposing a search size of 256 (128) and a reference size of 64 (32) pixels for high (low) displacement values. Finally, the movement rates obtained by manual feature identification and by the feature-tracking algorithm were compared against 54 GNSS points distributed on the rock glacier.

# 4. Results

## 4.1 Frozen and unfrozen ground conditions

Figure 2a shows the inverted ERT results for the white lobe (sector III), GRS-LW. The specific resistivity distribution shows two high-resistive bodies in the central (~30m thickness) and downslope (~20 m thickness) part of the rock glacier. Below these anomalies, which are interpreted as substantial frozen ground occurrences, the resistivity values decrease again suggesting unfrozen ground conditions. The high-resistive, frozen part is overlaid by a less resistive surface layer representing the active layer. Resistivity values < 5 kohm-m at depth, between 0 and 120 m horizontal distance, indicate the unfrozen conditions in the upper part of the rock glacier caused by the LIA glacier overriding.

Along the longitudinal profile on the black lobe (sector II) a continuous layer (20 m thick) with high resistivity values is present along the whole profile length (Figure 2b). The GRS-LB profile is shorter and has a smaller penetration depth than GRS-LW due to the smaller electrode spacing (5 m instead of 10 m for the white lobe). Maximum resistivity values are slightly larger and more homogeneous for the black lobe (~100 kohm-m) indicating a potentially slightly higher ice content.

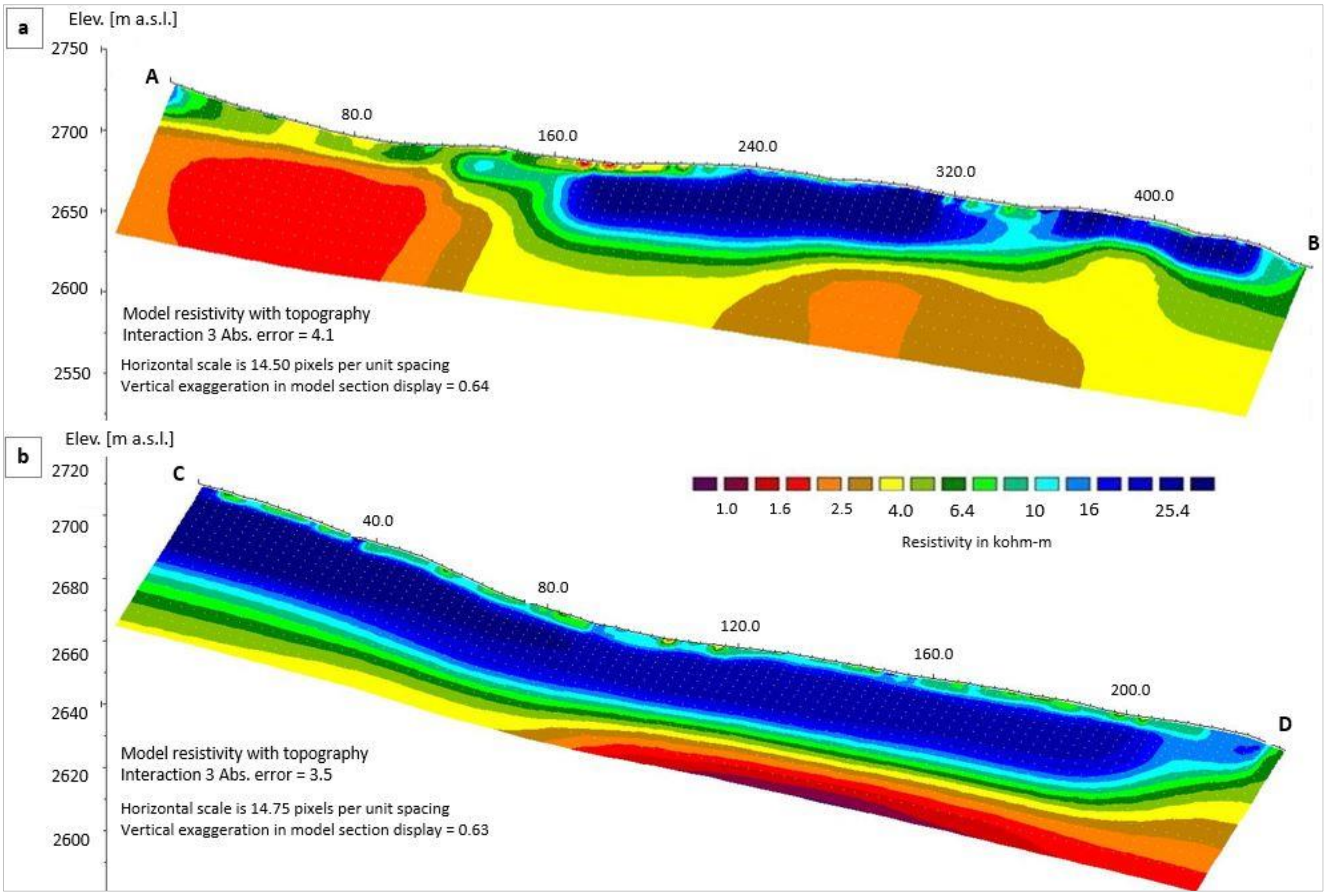


Figure 2. (a) Inverted specific resistivity distribution for profile GRS-LW from 22.7.2015 with an electrode spacing of 10 m; (b) Inverted specific resistivity distribution for profile GRS-LB from 23.7.2015 with an electrode spacing of 5 m.

## 4.2 Accuracy of point clouds and orthophotos

The accuracy of point clouds and orthophotos is assessed by computing the RMSE, mean error and standard deviation of both GCPs, used for model generation, and CPs, used for the assessment of model accuracy (Table 2). The GCP RMSE is less than 4.18 cm for all years except for the 2015 point cloud where the error is 13.63 cm. The RMSE of CPs are 5.24 cm (2016), 4.68 cm (2017), 9.34 cm (2018) and 3.51 cm (2019) whereas in the year 2015 the CP RMSE is 26.15 cm.

In Table 2, we present the values of *reg* (eq. 1) and $LOD_{95\%}$ (eq. 2) for each pair of data investigated in the 3D change analysis. The highest *reg* value (26.38 cm) is associated with the 2015-2019 comparison due to the lower accuracy of the 2015 dataset. In contrast, the lowest value (5.85 cm) occurs for the 2017-2019 interval, obtained by combining the lowest RMSE values. Since the *reg* is a prerequisite for the estimation of the level of detection, its value has implications in determining the $LOD_{95\%}$. The minimum $LOD_{95\%}$ (14 cm) is found for the 2017-2019 interval in which the point clouds used are the densest, about 35M and 24M points for 2017 and 2019, respectively. On the other hand, the highest threshold value, 55 cm for the 2015-2019 interval, is due to the 2015 low point cloud density (10M points) compared to 2019 (24M). The cloud densities refer only to the rock glacier outline (Figure 1c). In the end, *reg* and $LOD_{95\%}$ values are comparable for the time intervals 2018-2019, 2017-2019 and 2016-2019, while the 2015-2019 interval is the worst due to the limitations of the 2015 model.

| **year** | **GCP** | | | | | |
|---|---|---|---|---|---|---|
| | **RMSE xy (cm)** | **RMSE z (cm)** | **Total RMSE (cm)** | **ME │STDEV x (cm)** | **ME │STDEV y (cm)** | **ME │STDEV z (cm)** |
| **2015** | 10.59 | 8.58 | 13.63 | 0.02 │ 7.14 | -0.004 │ 8.79 | -0.04 │ 9.17 |
| **2016** | 3.36 | 2.49 | 4.18 | 0.31 │ 1.95 | -0.72 │ 2.81 | 0.27 │ 2.60 |
| **2017** | 2.46 | 2.87 | 3.78 | -0.56 │ 1.60 | 0.23 │ 1.93 | -0.34 │ 2.98 |
| **2018** | 2.48 | 3.07 | 3.94 | 0.03 │ 1.50 | -0.002 │ 2.11 | -0.08 │ 3.20 |
| **2019** | 2.26 | 1.45 | 2.69 | -0.27 │ 1.90 | 0.11 │ 1.37 | -0.07 │ 1.51 |
| | **CP** | | | | | |
| | **RMSE xy (cm)** | **RMSE z (cm)** | **Total RMSE (cm)** | **ME │STDEV x (cm)** | **ME │STDEV y (cm)** | **ME │STDEV z (cm)** |
| **2015** | 21.05 | 15.51 | 26.15 | 10.94 │ 13.78 | 1.01 │ 14.03 | 1.73 │ 16.88 |
| **2016** | 3.31 | 4.06 | 5.24 | 0.06 │ 2.62 | 0.03 │ 2.51 | -1.16 │ 4.26 |
| **2017** | 2.26 | 4.10 | 4.68 | 0.84 │ 1.71 | -0.40 │ 1.38 | -0.68 │ 4.33 |
| **2018** | 2.72 | 8.94 | 9.34 | -0.03 │ 1.32 | -0.09 │ 2.60 | 3.79 │ 8.65 |
| **2019** | 1.76 | 3.04 | 3.51 | -0.15 │ 1.56 | 0.11 │ 1.08 | 0.33 │ 3.26 |
| | | | | | | |
| | | **Time interval** | **Registration error (cm)** | | **$LOD_{95\%}$ (cm)** | |
| Rock glacier (I + II + III+ IV) | | **2015-2019** | 26.38 | | 55 | |
| | | **2016-2019** | 6.31 | | 16 | |
| | | **2017-2019** | 5.85 | | 14 | |
| | | **2018-2019** | 9.98 | | 22 | |

Table 2. Root mean square error (RMSE), mean error (ME) and standard deviation (STDEV) for both GCP and CP. Registration error and level of detection threshold for each time interval investigated.

### 4.3 3D surface changes

The description of the surface changes of the Gran Sometta rock glacier is based on the products derived from dense cloud-to-cloud comparisons.

As shown in Table 3, for the three most recent intervals (2018-2019, 2017-2019 and 2016-2019) the significative surface change areas (i.e. areas statistically significant at 95% confidence) increase as the time interval increases, spanning from 14% to 44% of the rock glacier area. Unexpectedly, the percentage of surface changes for the 4-year comparison (2015-2019) is only 25%. This can be explained by the relatively low geometric accuracy and low point cloud density of the year 2015 compared to the most recent surveys, affecting the significance of the quantified surface changes.

The surface changes are indicated with “negative surface changes” for surface lowering and mass loss processes whereas “positive surface changes” indicate accumulation processes and mass gain due to the advance of the rock glacier. The statistically significant surface changes are mostly negative, between 65 and 68%. Only for the 2018-2019 comparison there is a predominance of positive (52%) over negative (48%) changes.

| **Time interval** | **Areas of significant surface changes (%)** | **Mean significant surface change (m)** | **Areas of positive surface changes (%)** | **Areas of negative surface changes (%)** | **Mean positive surface change (m)** | **Mean negative surface change (m)** |
|---|---|---|---|---|---|---|
| 2015-2019 | 25 | -0.11 | 34 | 66 | 1.70 | -0.93 |
| 2016-2019 | 44 | -0.03 | 35 | 65 | 0.73 | -0.44 |
| 2017-2019 | 36 | -0.11 | 32 | 68 | 0.47 | -0.38 |
| 2018-2019 | 14 | 0.07 | 52 | 48 | 0.48 | -0.39 |

Table 3. Percentage of areas and absolute mean significant surface changes reported for the investigated time intervals. These variations were divided into positive and negative significant areas (with associated percentages and absolute mean values) for material gain and material loss, respectively.

Here, the comparison is limited to the period 2016-2019. The 2015 survey is excluded since characterized by the highest RMSE, hardly comparable with those of the following/subsequent years. In Figure 3, we present the rock glacier areas characterized by significant changes between 2016 and 2019, generated by comparing point clouds via the M3C2 plug-in.

Distinct longitudinal and transverse positive and mostly negative distance changes occur on the main part of the rock glacier as a result from advancing ridges and furrows. The alternating spatial pattern of mass gains and losses mostly indicates a downslope propagation of material from the upper zones of the rock glacier. Accumulation processes are less frequent and occur mostly in the frontal lobes and less in the ridge and furrows systems. The upper part (sector IV) of the rock glacier shows non-significant variations in accordance with the almost stable behaviour of the sector over time (i.e., minimal displacements, and negligible morphological changes).

Considering the 2016-2019 range, the areas with significant changes cover 45% of the external lobe, 31% of the black lobe, 23% of the white lobe and only 1% in the upper part where there is no subsurface. Negative vertical changes dominate in all sectors with the exception of the lowest parts of the external and black lobes where continued advance of the creeping frozen ground is documented.

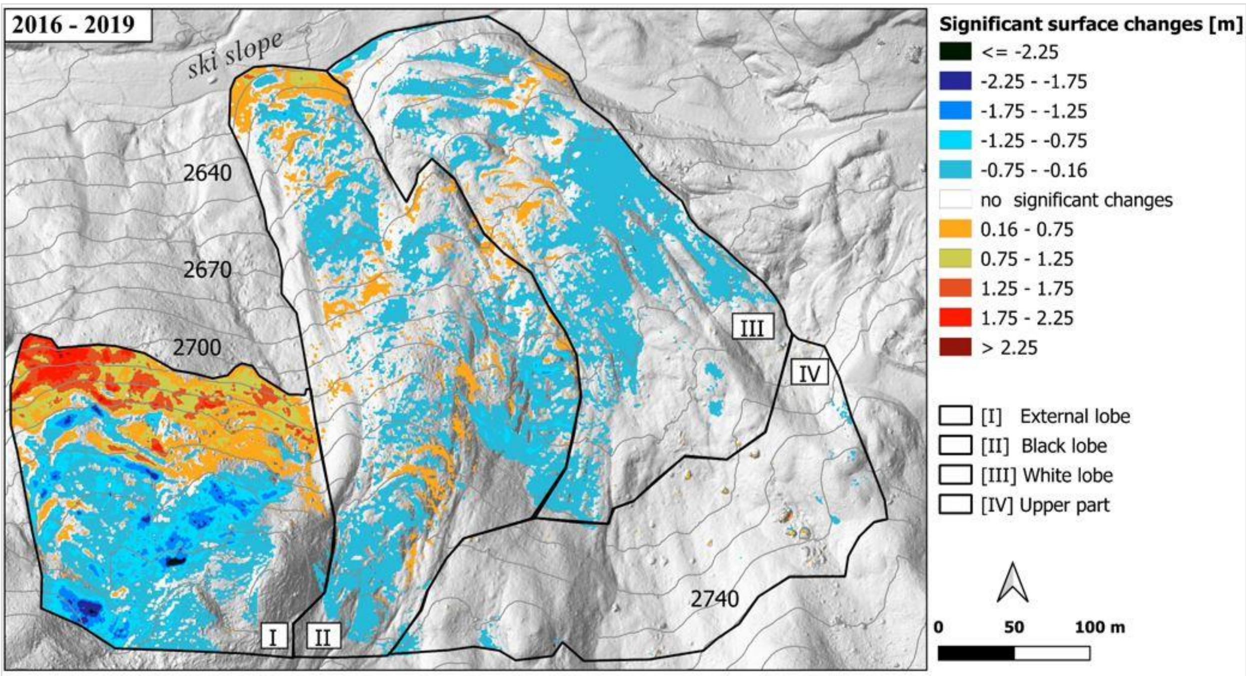


Figure 3 Rock glacier areas characterized by significant changes between 2016 and 2019, generated by 3D point cloud comparison with the M3C2 plug-in.

At the front of the external lobe (sector I), the positive surface change values are above 0.75 m, with larger variations in the westernmost part. The upstream negative changes reached values greater than -0.75 m. Less intense surface changes characterise the black (sector II) and white (sector III) lobes. Alternate positive and negative changes up to 0.75 m occur in the furrow and ridge areas (especially in the upper part of sector II). Considering only the statistically significant surface changes in the period 2016-2019, the negative changes correspond almost to the totality (89%) of the changes estimated on the white lobe, to the 68% on the black lobe and 51% of the external lobe. The upper part (sector IV) is not considered since the percentage of significant areas is lower than 1%.

Differences between rock glacier sectors are further analysed on an annual basis using the empirical cumulative distribution function - ECDF (Figure 4), by subtracting products derived from the M3C2 distance map. The line referring to the zero of M3C2 distance on the x-axis (unrealistic condition in which no change occurs) intercepting the ECDF curves defines the percentage of area points subject to real negative vertical changes (negative M3C2 values). The remaining percentage corresponds to the positive vertical changes, the intensity of which is represented by the part of ECDF curves to the right of the straight line.

The external lobe (Figure 4a) is subject to slight positive changes in 2016-2017 and 2018-2019 period whereas a net predominant negative surface change (~ 70% of the area) occurs in 2017-2018. A similar tendency is observed for the black lobe (Figure 4b) where major negative changes occur again in 2017-2018, with changes affecting 80% of the area. Similar trends are observed in 2016-2017 and 2018-2019 periods, with a slight predominance of positive changes (~ 51%). Considering the white lobe (Figure 4c), negative changes predominate in all years, above 60% for the 2016-2017 and 2018-2019 and about 55% in 2017-2019.

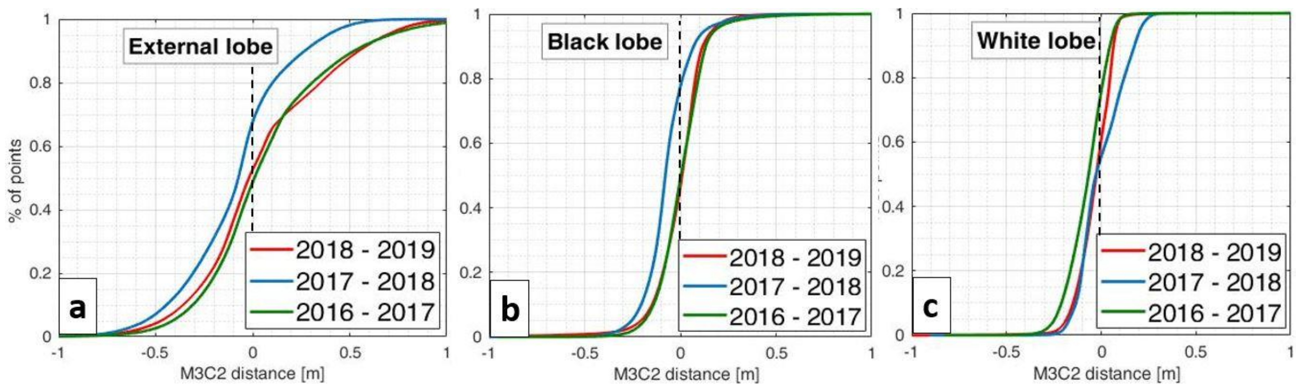

Figure 4. Annual empirical cumulative distribution functions (ECDF) for the three main sectors of the rock glacier (see fig. 1c), elaborated from the M3C2 distance products: (a) external lobe; (b) black lobe; (c) white lobe.

### 4.4 Analysis of displacement vectors

The horizontal surface velocities were computed identifying corresponding features manually on the orthophotos through time and using the automatic IMCORR feature-tracking algorithm. These results were then compared against repeated GNSS measurements, considered here as a reference.

The displacement vectors resulting from the manual identification of corresponding features enable the identification of different spatial patterns of surface velocity (Figure 5a). Considering the period 2015-2019, the rock glacier shows a clear distinction in creep dynamics between a faster western part and a slower eastern part, as already demonstrated in the previous analyses. Analysing the interannual variability (Figure 5c), the black and white lobes show the highest mean horizontal surface velocity in the period 2014-2015 (> 1.4 m/y on the black front and ~ 0.5 m/y in the central part of the white lobe) and a progressive decrease culminating in 2017-2018 when minimum velocities are recorded. The following year (2018-2019) is marked by an increase in surface velocity, especially on the black lobe. Here the maximum horizontal displacement rates are recorded at the front part (1.30 m/y) while in the adjacent lobe velocities are slightly lower than 0.5 m/y. The external lobe, with average values of 1.7 m/y, also shows an increase in surface movements in the year 2018-2019.

A further evaluation of the surface displacement field was performed based on repeated GNSS campaigns performed on 54 points distributed over the rock glacier (Figure 1c). The interannual surface velocity (Figure 5c) was estimated between 2012 and 2020 for the black (sector II) and white (sector III) lobes and from 2015 to 2020 for the external lobe (sector I). An increase in interannual surface velocity of the rock glacier between 2013 and 2015 can be observed, from a maximum of around 1.1 m/y for the black lobe in 2013 to an average value of more than 1.4 m/y in 2015. Between 2015 and 2018, the velocity decreased compared to the surface velocities recorded in the period 2013-2015. From 2018, flow velocity increased again until 2020 with maximum values of 0.4 m/y (white lobe), 1.3 m/y (black lobe) and 1.9 m/y (external lobe).

The velocity patterns generated with the image correlation algorithm and referring to the period 2015-2019 are represented in figure 5b together with the displacements detected by the GNSS measurements.

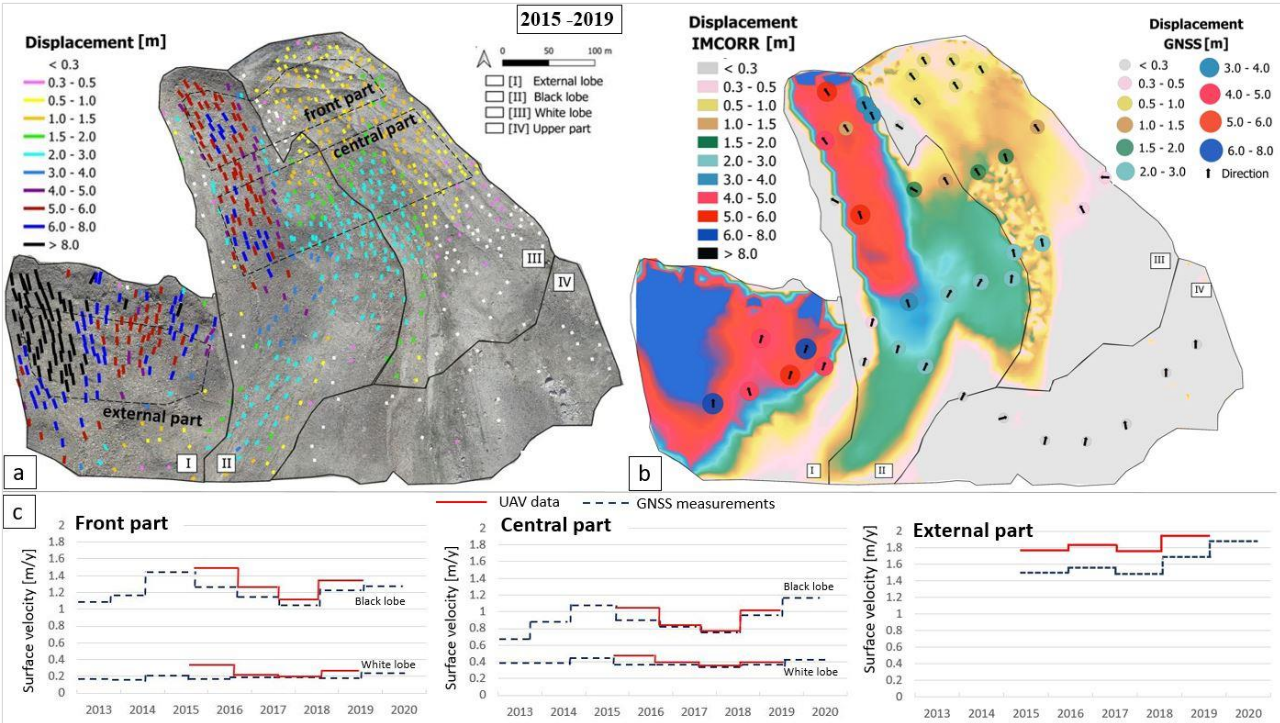


Figure 5. (a) Horizontal displacement magnitudes between 2015 and 2019, obtained by manual measurements on orthophotos. (b) Horizontal displacement magnitudes derived from IMCORR image correlation algorithm and GNSS measurements within the period 2015-2019. (c) Annual horizontal surface velocities of the rock glacier detected by UAV measurements (red line) and by GNSS measurements (blue dotted line). The mean of the polygons (front part, central part, and external part) shown in (a) are reported for each sector.

The horizontal displacements measured at the marker points by GNSS were compared to the horizontal displacements derived by manual feature identification on the orthophotos (Figure 6a) and by IMCORR image correlation algorithm from UAV data (Figure 6b). GNSS measurements agree well with the manual feature identification approach and the image correlation algorithm. The results from the image correlation algorithm are better related to GNSS measurements ($R^2$ = 0.99 and RMSE = 0.04-0.07 m/y) than those from manual feature identification ($R^2$ = 0.96-0.98 and RMSE = 0.09-0.12 m/y).

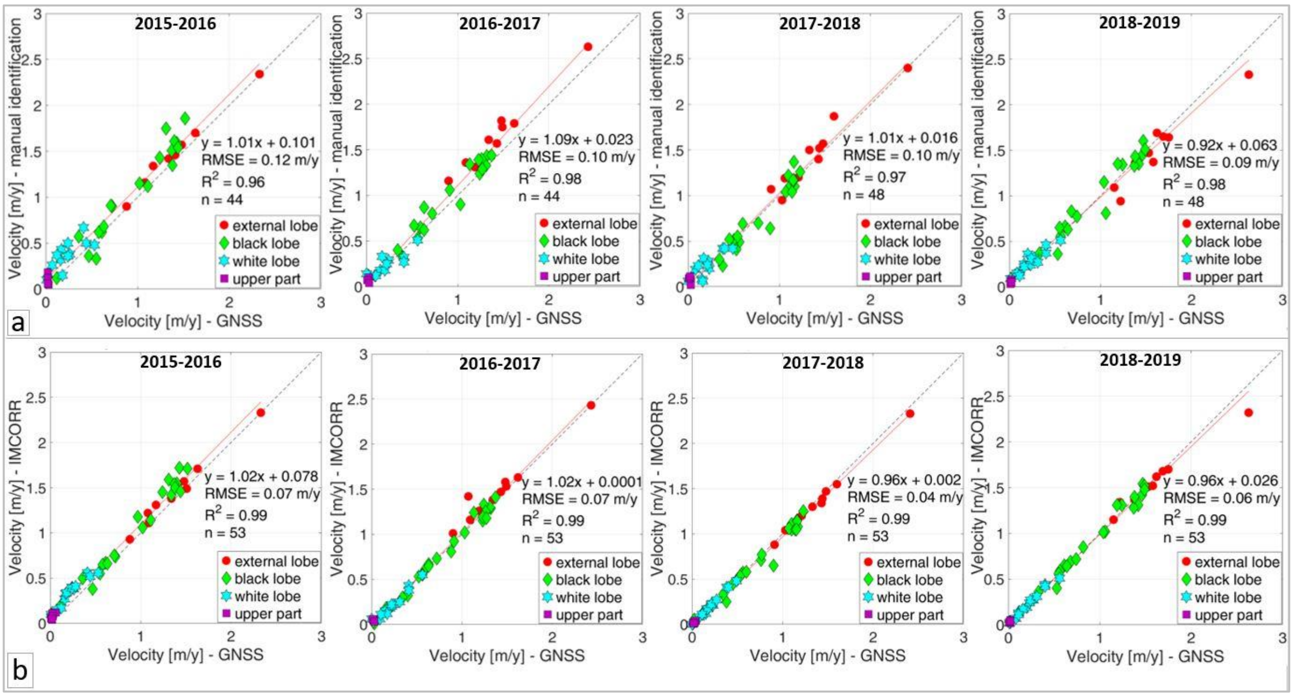


Figure 6. Scatterplots between displacements obtained from (a) manual orthophotos comparison and GNSS measurements and (b) image correlation algorithm and GNSS measurements.

## 4.5 Surface elevation changes

Two approaches are adopted to map and quantify the surface elevation changes of the rock glacier, i.e. the classic difference of DSMs (DoD) and the Nz component, which is one of the products (together with Nx and Ny components) resulting from the decomposition of the M3C2 distance map.

The DoD and Nz maps provide the spatial distribution of topographic change through time. The result represent decrease and increase in elevation as negative and positive values, respectively. DoD shows a mean ± standard deviation equal of -0.05 ± 0.4 m while for the Nz component is -0.07 ± 0.3 m. The spatial patterns observed in the DoD map are similar to those described in the Nz map even if in the first case more features are highlighted by more pronounced vertical changes. This difference is due to the M3C2 algorithm that tracks 3D variations in surface orientation with respect to the changes in the z direction only computed by classic DoD approach. This is observed both in the white lobe and in the black lobe, at around 2680 m. a.s.l. Here, less changes in elevation are mapped indicating that the z-component is not the main one in that sector for the period 2016-2019 where instead horizontal ones predominate.

Figure 7 shows the comparison between maps of DoD and Nz component in the 2016-2019 period.

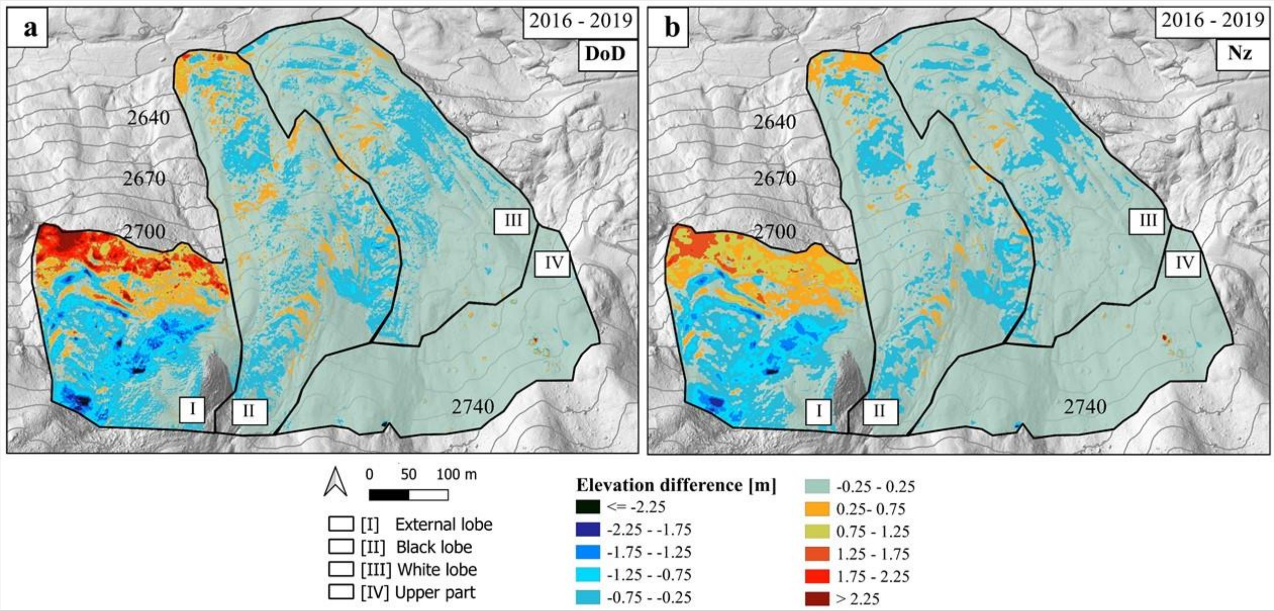


Figure 7. (a) Vertical differences obtained through DSM differencing (DoD) and (b) dense point cloud comparison, considering the vertical component of the normal surface in the reference point cloud (Nz). The time investigated covers the period from August 2016 to August 2019. The hillshade refers to the year 2016.

## 4.6 Interannual variability of GST measurements and meteorological data

Parameters derived from GST measurements (Fig. 1c for locations) as the MAGST, the GFI, the GTI and the WEqT as well as the duration of snowmelt period and mean air temperature (mean $T_{air}$) are shown in table 4.

MAGST varies between 0.70 °C and 2.04 °C, with values higher than 1.6 °C in years when an increase in horizontal surface velocity is observed, 2014-2015, 2018-2019 and 2019-2020. While the GTI does not seem to give a kinematic response, the GFI conditions above -0.6 °C are characterized by an increment in surface velocities whereas colder GFI results in a decrease in surface displacements as between 2015 and 2018. The WEqT varies between -1.18 °C and -1.96 °C with values higher than -1.4 °C in years with increased surface velocities and values lower than -1.7 °C in years characterized by a decreasing velocity process (2015-2016, 2016-2017 and 2017-2018). Thus, changes in surface displacement rates in the period 2014-2020 can be interpreted to be caused by variations in GST-based parameters, while snowmelt period and $T_{air}$ did not seem to directly affect rock glacier creep rate.

| **Year** | **MAGST [°C]** | **GFI [°C]** | **GTI [°C]** | **WEqT [°C]** | **mean $T_{air}$ [°C]** | **Snowmelt period [start-end]** |
|---|---|---|---|---|---|---|

| | | | | | | |
|---|---|---|---|---|---|---|
| **2014-2015 (*)** | 2.04 | -0.34 | 2.12 (2015) | -1.24 (2015) | 6.23 (2015) | 22 April - 16 June (2015) |
| **2015-2016** | 0.70 | -1.07 | 1.90 (2016) | -1.96 (2016) | 6.29 (2016) | 12 May - 26 June (2016) |
| **2016-2017** | 1.36 | -0.76 | 2.07 (2017) | -1.83 (2017) | 6.15 (2017) | 13 April – 17 June (2017) |
| **2017-2018** | 0.80 | -1.12 | 2.22 (2018) | -1.77 (2018) | 6.88 (2018) | 24 April – 28 June (2018) |
| **2018-2019 (*)** | 1.68 | -0.52 | 2.10 (2019) | -1.18 (2019) | 6.79 (2019) | 24 May – 30 June (2019) |
| **2019-2020 (*)** | 1.91 | -0.30 | / | -1.40 (2020) | / | 19 April – 26 June (2020) |

Table 4. MAGST (Mean Annual Surface Temperature); GFI (Ground Freezing Index); GTI (Ground Thawing Index); WEqT (Winter Equilibrium Temperature); mean air temperature (mean Tair) from June to September; duration of snowmelt period [start of snowmelt and snow free date]. Period from 2014 to 2020. The asterisk (*) indicates the years of largest rock glacier creep velocity.

## 5. Discussion

The multi-temporal kinematics of the Gran Sometta rock glacier surface was analysed through five UAV campaigns (2015–2019) and annual GNSS surveys from 2012 to 2020 and discussed hereafter considering the ERT tomograms and GST data.

### 5.1 Level of detection assessment and 3D geomorphological activity quantification

In this study, beside the difference between DSMs, a point cloud-based distance calculation algorithm is applied, and 3D surface changes are quantified on pairs of UAV acquisitions. Moreover, the ability of the 3D change analysis to reliably quantify topographic changes is assessed by statistically evaluating the confidence interval of the estimated distance, also referred to as the level of detection (LOD) at 95%, for each of the multi-temporal pair of acquisitions. We compared our $LOD_{95\%}$ values with those found by Zahs et al. (2019) and Bollmann et al. (2012) on other rock glaciers. For an annual interval, the $LOD_{95\%}$ of surface changes quantified by Zahs et al. (2019) is 9 cm and more than 30 cm in Bollmann et al. (2012), while in our case the $LOD_{95\%}$ value is 22 cm. However, it should be noted that both Zahs et al. (2019) and Bollmann et al. (2012) used multi-temporal Airborne Laser Scanning (ALS) point clouds in their studies. Furthermore, Zahs et al. (2019) missed an independent evaluation of the geometric accuracy of the ALS products, hampering a proper comparison with the results obtained in this work.

For the 2018-2019, 2017-2019 and 2016-2019 intervals the areas of the rock glacier with significative surface change increase with the time interval, spanning from 14% in one year, to 36% in two years and to 44% in three years. Conversely, the percentage of surface changes for the 4-year comparison (2015-2019) is only 25% due to low geometric accuracy and low point cloud density of the year 2015 compared to the most recent surveys.

Surface elevation changes estimated with DoD and through the decomposition of the M3C2 distance map to obtain its vertical component (Nz) show similar spatial patterns (see Fig. 7a and Fig. 7b) even if in the latter case few features with less pronounced vertical changes are highlighted. A clear example concerns the white and black lobes in which it is possible to highlight a portion where fewer vertical changes are detected. This indicates that in this area and for the time interval under consideration, the z component of the displacements is secondary to the predominant horizontal one. This depends on the M3C2 algorithm which computes the local distance between two point clouds along the normal surface direction which tracks 3D variations in surface orientation (Lague et al., 2013) and not only with respect to the z direction as in the classic DoD approach. Moreover, compared to DoD, the M3C2 algorithm operates directly on point clouds without meshing or gridding, and thus, reduces the uncertainty related to missing data and interpolation errors. These errors can be particularly relevant in landscapes characterized by rough morphology, such as rock glaciers, since the DSM decreases information density proportionally to surface steepness (Zahs et al., 2019). To confirm this, the overall greatest difference between the methods is found in the sector with the highest slope gradient, i.e. in the external lobe (~ 27°), and less pronounced changes in the white lobe, which is characterized by a 20° slope gradient. Furthermore, we recorded the maximum velocities in the steeper sector (external lobe), while in the white lobe, with the lowest average slope, we observed the smallest velocity range. Spatial patterns of rock glacier properties and dynamics can be explained by several factors (Cicoira et al., 2020; Müller et al., 2016; Bodin et al., 2018). Combining a model for calculating rock glaciers thickness with an empirical model of ice-rich debris creep, Cicoira et al. (2020) derived a Bulk Creep Coefficient (BCF) which allows to explain the contribution of material properties and geometry to surface velocities. For dynamically non-destabilized rock glaciers, Cicoira et al. (2020) shows that the geometry seems to demonstrate spatial variability of flow rates with almost constant rheological properties of the debris. Müller et al. (2016) analysed two rock glaciers in the Swiss Alps and observed that the steeper rock glacier showed flow velocities (0.75-1.55 m/y) higher than the gentler rock glacier (0.06-0.13 m/y). Analysing the entire profile of the Laurichard rock glacier, in the French Alps, Bodin et al. (2018) did not find a clear control of slope on surface velocity but, considering only a limited sector of it, they detected a significant relationship between rock glacier velocity and slope gradient higher than 20°.

### 5.2 Interannual velocity variations

Time series of rock glacier movement in the European Alps indicate an acceleration in permafrost creep in recent decades in relation to an increase in permafrost temperatures and water content (Kenner et al., 2019). Although changes in ice properties due to permafrost degradation appear to significantly influence rock glacier kinematics, the factor that may trigger rock glacier destabilisation remains a source of debate (Vivero & Lambiel, 2019).

Annual surveys conducted at several rock glaciers in the European Alps suggest an increase in mean surface velocity of +52% during the 2010-2014 period with most of them reaching maxima in 2014 (PERMOS, 2016; Delaloye et al., 2013). A new maximum velocity peak was reached in 2015, followed by a progressive decrease of the creep velocities until 2017-2018, with an average reduction of surface velocities of -28% in the Swiss Alps (PERMOS, 2019). A new gradual increase in surface movement rates is observed since 2018. Considering the period 2012-2020, the interannual flow velocity of the Gran Sometta rock glacier shows a trend similar to the one descried by PERMOS. The maximum surface velocity was reached in 2015, followed by a decrease until 2017-2018 in which the minimum average values of 0.2 m/y for the white lobe, 0.75 m/y for black lobe and 1.5 m/y for the external lobe were detected. A gradual increase in horizontal surface velocity has been observed since 2018 with peak values of 0.4 m/y, 1.2 m/y and 1.9 m/y for the white, black, and external lobes respectively, in 2020.

In this study, different methods for the estimation of rock glacier velocities were applied. Displacement vectors from GNSS measurements provide accurate information but are limited to 54 points on the rock glacier surface. On the other hand, the displacement vectors derived from UAV surveys allowed a better characterization of the spatial variability of rock glacier displacements. In particular, the image correlation algorithm allows the generation of velocity maps on a regular spatial grid, allowing the identification of areas moving at different velocities. The results from the image correlation algorithm are better related to GNSS measurements ($R^2$ equal to 0.99 and RMSE between 0.04 m/y and 0.07 m/y) than those from manual feature identification ($R^2$ between

0.96 and 0.98 and a RMSE between 0.09 m/y and 0.12 m/y). The lower accuracy when estimating surface velocities through manual feature identification can be explained by (i) errors in the manual identification of some points and (ii) non-coincidence between manual points and GNSS data that made it necessary to average the points from manual identification closer to the GNSS points.

**5.3 ERT interpretation and permafrost characteristics**

Several studies highlighted that the spatial patterns of rock glacier dynamics are largely controlled by the internal structure and by the thickness, ice content and temperature of the frozen body (Cicoira et al., 2020; Fey et al., 2020; Cicoira et al. 2019; Kenner et al., 2019). The viscous flow patterns of the rock glacier are due to the presence of a thick and continuous perennially frozen layer supersaturated with ice (Haeberli and Vonder Mühll, 1996). The Gran Sometta rock glacier reveals a complex dynamics linked to the heterogeneous distribution of perennially frozen debris rich in ice and thick enough (about 20-30 metres) for permafrost creep to occur. Along the white lobe (GRS-LW), the upper part of the profile, interpreted as unfrozen from the ERT results, corresponds to a sector where no movements are detected by cloud-to-cloud and manual feature identification on orthophotos. The absence of any significant movement in the upper part (sector IV) is related to the lack of permafrost in this area probably related to the development and advance of a small glacier, not heavily charged with debris, during the Little Ice Age. The unfrozen layer may be indicative of (i) degradation of former permafrost by a temperate small LIA glacier or (ii) mechanical effect of the LIA glacier that pushed the permafrost to unfavourable positions to its preservation (Delaloye and Lambiel, 2008). However, in the central and lower part of this profile, we identified the presence of two distinct frozen ground bodies, with a thickness of around 30 m and 20 m for the upper and the lower one respectively. An increase in surface horizontal velocity is observed in this zone. Additionally, the slower eastern part is not only gentler, but it also largely corresponds to currently degrading permafrost, where a thaw induced subsidence of up to 5 cm/y is observed.

A different situation is found for the slightly faster moving black lobe, where a continuous perennially ice-rich frozen ground body with a thickness of approximately 20 m is detected over most of the profile length (GRS-LB). The occurrence of subsurface frozen sediments, without any massive ice layer close to the surface, correspond to the zone not covered by a glacier during the LIA (Delaloye and Lambiel, 2008). The creep behaviour of subsurface ice-rich frozen layers depends mainly on the ice content and on the size of the grains that constitute the debris material (Cicoira et al., 2020). Imposed stresses and deformations in active rock glaciers affect the microscopic structure of the ice-debris mixture involved (Haeberli and Vonder Mühll, 1996). Hence, we suggest that the different velocities recorded at the two lobes stem hereby from the heterogeneous distribution of frozen ground, as visualized by the geophysical measurements.

Borehole data (provided by the Environmental Protection Agency of Valle d'Aosta but not shown here) show that the entire active layer is freezing each winter. However, the ice-rich perennially frozen debris documented by the ERT profiles are close to thawing conditions. The investigated permafrost is undergoing a degradation phase, like probably most permafrost occurrences in the Alps and comparable mountain environments and appears to be in strong imbalance with the current climatic conditions. Overall, the structure and thermal state of frozen ground at depth, but also the topographical settings appear as the main factors explaining the current flow patterns of the Gran Sometta rock glacier. On the contrary, the high interannual variations of creep rates in perennially frozen debris of rock glacier are likely to be related to external climatic factors rather than to local internal characteristics of the rock glacier permafrost.

**5.4 Permafrost thermal regime**

Recent studies showed that annual variations in rock glacier surface velocities can be related to GST variations. GST variations reflect, with a delay of several months, the variations of the temperature of the upper permafrost layers due to the slow propagation of annual surface thermal anomalies deeper into the permafrost (Staub et al., 2016; Delaloye et al., 2010). Several studies showed that the surface thermal signal can usually penetrate to permafrost layers located at 10-30 m depth (Staub et al., 2016; Delaloye et al., 2010). Interannual surface velocity variations have been shown to follow an exponential relation with multiannual GST forcing (Staub et al., 2016), as in the case of the Becs-de-Bosson rock glacier (in the Valais Alps) where most of the inter-annual velocity variations during one decade were related to temperature changes at 10-30 m depth. On the Dösen rock glacier (central Austria), Kellerer-Pirklbauer and Kaufmann (2012) observed that a reduction by 50% of the freezing-degree days at one meter depth causes a velocity increase by 1.5 times.

The active layer temperatures are influenced by the multi-annual mean annual air temperature (MAAT) trend. The increase in MAAT may delay the freezing of the active layer, produce early melting of spring snow, and consequently promote a rapid acceleration of creep rates (Kenner et al., 2019; Bonnaventure and Lamoureux, 2013). In addition, the relationship between snow cover and permafrost creep rates indicates a long-term delay in surface velocity caused by snow melting and water percolation into the perennially frozen material and storage of water for weeks to months favouring faster creep movement within the rock glacier with a significant time lag (Kenner et al., 2019). Kellerer-Pirklbauer et al (2017) show that over the period 2007-2015 a significant permafrost warming inside a rock glacier body caused an acceleration of surface flow velocity over the last two decades.

The comparison with air temperature data revealed a time lag of one to more years for acceleration caused by warm air temperatures (Kellerer-Pirklbauer and Kaufmann, 2012). In contrast, strong cooling causes a slightly faster deceleration possibly related to the reduced availability of liquid water within the rock glacier. These observations show that warmer air temperature, warmer GST, and warmer permafrost temperature favour creep acceleration. Long periods of warm surface conditions cause rising permafrost temperature and accelerated creep rates in rock glacier permafrost. The snow cover and its onset in early winter have a greater influence on the heat and energy exchange at the ground surface than air temperatures whose effect is limited to the snow-free period (Staub et al., 2016; Kenner et al., 2019).

In our study, the observations over a short-term period (2014-2020) suggest that the increase in creep rates of rock glacier permafrost depends on the ground thermal regime and on the related permafrost warming rather than directly on air temperatures, and timing and duration of snow melt period. A MAGST value higher than 1.6°C is found as a recurring parameter in years when an increase in horizontal surface velocity is observed (2014-2015, 2018-2019 and 2019-2020). While the GTI does not seem to play a role on the observed rock glacier creep rate variations, GFI values seems to be related to the observed kinematic responses. Indeed, years with GFI conditions above -0.6°C are characterised by an increment of surface velocities, while colder GFI result in a decrease in surface displacements. Increase and decrease in surface velocities generally correspond to WEqT values greater than -1.4°C and lower than -1.7°C, respectively. Thus, we hypothesized that the increase in horizontal velocities of the investigated rock glacier (2014-2015, 2018-2019 and 2019-2020) can be related to warm surface conditions. In fact, the highest measured values of MAGST (> 1.6°C), GFI (> -

0.6°C), and WEqT (> -1.4°C) correspond to an acceleration phase of creep within the rock glacier permafrost. Inversely, ground cooling causes a slight deceleration of creep rates as in the period from 2015 to 2018 where the MAGST, the GFI and the WEqT are slightly lower (< 0.7°C, < -0.8°C and < -1.8°C respectively) than in the acceleration phase.

The present study illustrates that permafrost continues to exist also when local glaciers have long disappeared. Rock glaciers with their debris cover are usually more resilient and respond to climate change on relatively longer time scales than glaciers (Haeberli et al., 2006), which with their evolution are considered excellent climate change indicators. This is due to the fact that the characteristic range of permafrost thaw rates is by one to two orders of magnitude lower than present-day melt rates of glaciers. With the current warming rate (temperatures have risen by 2°C in the European Alps over the 20$^{th}$ century, Gobiet et al., 2014), a century will maybe enough for a complete thaw of the investigated permafrost at Gran Sometta rock glacier. With positive mean annual surface temperatures and presumably accelerated future atmospheric warming, many other rock glaciers may suffer the same fate as observed on the Gran Sometta.

## 5. Conclusions

This work enabled the quantification and interpretation of the kinematics of the Gran Sometta rock glacier permafrost and its downstream movement using multi-temporal UAV acquisitions, GNSS surveys, geophysical prospections, and GST measurements. UAV acquisitions allowed the characterization of the spatial distribution of surface displacements even in inaccessible site as opposed to GNSS surveys which provide high accurate information but limited on a few selected points on the surface. The M3C2 distance calculation algorithm is a valid tool to calculate mass transport processes with complex geomorphology and it was successfully adapted to quantify the surface normal thickness changes of the Gran Sometta rock glacier.

The interannual changes in creep rates of the rock glacier permafrost are in agreement with the trend observed in other Alpine rock glaciers. Considering 2012-2020, maximum peak surface velocities were reached in 2015, followed by a velocity decrease until 2017-2018 but the following two years (2018-2019 and 2019-2020) are marked by a gradual increase in surface velocity.

Processes of freezing and melting of the permafrost are influenced by a complex function of both rock glacier flow dynamics and ground thermal conditions. At Gran Sometta, the heterogeneous distribution of frozen ground occurrence at depth, its structure, and the topographical settings seem to be key factors explaining the observed spatial flow pattern. Annual kinematics are related to the ground thermal regime, as evinced by the MAGST, GFI and WEqT values. Increases in permafrost creep rates (in 2014-2015, 2018-2019 and 2019-2020) respond to higher MAGST values while a deceleration phase occurred with lower MAGST values as in 2015-2016, 2016-2017 and 2017-2018. Also, GFI and WEqT values higher than -0.6°C and -1.4°C, respectively, generally correspond to high surface displacement rates. The subsurface ice documented by ERT profiles is close to melting conditions and the investigated permafrost appears to be in imbalance with the current climatic conditions. The observed rates of thaw subsidence at the margins of the rock glacier active part, in the range of centimetres per year, are characteristic for ice-rich permafrost within rock glacier landforms.

**Acknowledgments**

This research is funded by the Italian MIUR project Dipartimenti di Eccellenza (2018-2022) and has been supported by the GEMMA (Geo Environmental Measuring and Monitoring from multiple plAtforms) laboratory of the University of Milano-Bicocca. The authors thank Dr. Wilfried Haeberli and an anonymous reviewer for valuable comments which helped to improve the manuscript.

**Bibliography**

Barsch, D., 1992. Permafrost creep and rock glaciers. Permafrost and Periglacial Processes, 3.3, 175-188.

Bauer, A., Paar, G., Kaufmann, V., 2003. Terrestrial laser scanning for rock glacier monitoring. Permafrost, Phillips, Springman & Arenson (Eds).

Bennet, M.R., 2001. The morphology, structural evolution and significance of push moraines. Earth Science Reviews, 53, 197-236.

Biskaborn, B.K., Smith, S.L., Noetzli, J., Matthes, H., Vieira, G., Streletskiy, D.A. et al., 2019. Permafrost is warming at a global scale. Nat. Commun., 10 (264). Doi: 10.1038/s41467-018-08240-4.

Bodin, X., Thibert, E., Sanchez, O., Rabatel, A., Jaillet, S., 2018. Multi-annual kinematics of an active rock glacier quantified from very high-resolution DEMs: an application-case in the French Alps. Remote Sensing, 10, 547. Doi: 10.3390/rs10040547.

Bollmann, E., Klug, C., Sailer, R., Stötter, J., 2012. Quantifying rock glacier creep using airborne laser scanning: a case study from two rock glaciers in the Austrian Alps. Tenth International Conference on Permafrost (Salekhard, Russia), volume 1. Doi: 10.13140/RG.2.1.3249.5202.

Bonnaventure, P.P., Lamoureux, S.F., 2013. The active layer: A conceptual review of monitoring, modelling techniques and changes in a warming climate. Prog. Phys. Geogr., 37, 352-376. Doi: 10.1177/0309133313478314.

Buchli, T., Merz, K., Zhou, X., Kinzelbach, W., Springman, S.M., 2013. Characterization and monitoring of the Furggwanghorn rock glacier, Turtmann Valley, Switzerland: results from 2010 to 2012. Vadose Zone Journal, 12. Doi: 10.2136/vzj2012.0067.

Cicoira, A., Marcer, M., Gärtner-Roer, I., Bodin, X., Arenson, L., Vieli, A., 2020. A general theory of rock glacier creep based on in-situ and remote sensing observations. Permafrost and Periglacial Processes, 32, 139-153. Doi: 10.1002/ppp.2090.

Cicoira, A., Beutel, J., Faillettaz, J., Vieli, A., 2019. Water controls the seasonal rhythm of rock glacier flow. Earth and Planetary Science Letters, 528. https://doi.org/10.1016/j.epsl.2019.115844.

Dall'Asta, E., Forlani, G., Roncella, R., Santise, M., Diotri, F., Morra di Cella, U., 2017. Unmanned aerial systems and DSM matching for rock glacier monitoring. ISPRS Journal of Photogrammetry and Remote Sensing, 127, 102-114. http://dx.doi.org/10.1016/j.isprsjprs.2016.10.003.

Delaloye, R., Barboux, C., Morard, S., Abbet, D., Gruber, V., 2013. Rapidly moving rock glaciers in Mattertal. In: Graf C (ed) Mattertal - ein Tal in Bewegung. Publikation zur Jahrestagung der Schweizerischen Geomorphologischen Gesellschaft, St. Niklaus, pp 21–31.

Delaloye, R., Lambiel, C., Gärtner-Roer, I., 2010. Overview of rock glacier kinematics research in the Swiss Alps. Geographica Helvetica, 65, pp 135-145.

Delaloye, R., Lambiel, C., 2008. Typology of vertical electrical soundings for permafrost/ground ice investigation in the forefields of small alpine glaciers. In: Hauck, C., Kneisel, C. (eds), Applied Geophysics in Periglacial Environments, Cambridge University Press, 101-108.

Delaloye, R., Perruchoud, E., Avian, M., Kaufmann, V., Bodin, X., Hausmann, H., Ikeda, A., Kääb, A., Kellerer-Pirklbauer, A., Krainer, K., Lambiel, C., Mihailovic, D., Staub, B., Roer, I., Thibert, E., 2008. Recent interannual variations of rock glacier creep in the European Alps. In: Kane, D.L., Hinkel, K.M. (Eds.). 9th International Conference on Permafrost Fairbanks, Alaska, 343-348.

Endrizzi, S., Gruber, S., Dall'Amico, M., Rigon, R., 2014. GEOtop 2.0: simulating the combined energy and water balance at and below the land surface accounting for soil freezing, snow cover and terrain effects. Geoscientific Model Development, 7(6), 2831-2857.

Etzelmüller, B., Guglielmin, M., Hauck, C., Hilbich, C., Hoelzle, M., Isaksen, K., Noetzli, J., Oliva, M., Ramos, M., 2020. Twenty years of European mountain permafrost dynamics – the PACE legacy. Environmental Research Letters, 15, 104070. https://doi.org/10.1088/1748-9326/abae9d.

Fahnestock, M.A., Scambos, T.A., Bindschadler, R.A., 1992. Semi-automated ice velocity determination from satellite imagery. Eos, 73, 493.

Fey, C., Krainer, K., 2020. Analyses of UAV and GNSS based flow velocity variations of the rock glacier Lazaun (Ötztal Alps, South Tyrol, Italy). Geomorphology, 365. https://doi.org/10.1016/j.geomorph.2020.107261.

Fey, C., Rutzinger, M., Wichmann, V., Prager, C., Bremer, M., Zangerl, C., 2015. Deriving 3D displacement vectors from multi-temporal airborne laser scanning data for landslide activity analyses. GIScience & Remote Sensing, 52 (4), 437-461. Doi: 10.1080/15481603.1045278.

Gobiet, A., Kotlarski, S., Beniston, M., Heinrich, G., Rajczak, J., Stoffel, M., 2014. 21st century climate change in the European Alps-A review. Science of the Total Environment, 493, 1138-1151. http://dx.doi.org/10.1016/j.scitotenv.2013.07.050.

Haberkorn, A., Kenner, R., Noetzli, J., Phillips, M., 2021. Changes in ground temperature and dynamics in mountain permafrost in the Swiss Alps. Front. Earth Sci., 9, 626686. Doi: 10.3389/feart.2021.626686.

Haeberli, W., Hallet, B., Arenson, L., Elconin, R., Humlum, O., Kääb, A., Kaufmann, V., Ladanyi, B., Matsuoka, N., Springman, S., Vonder Mühll, D., 2006. Permafrost creep and rock glacier dynamics. Permafrost and Periglacial Processes, 17/3, 189-241. Doi: 10.1002/ppp561.

Haeberli, W., Beniston, M., 1998. Climate change and its impact on glaciers and permafrost in the Alps. Ambio 27, 258-265. http://www.jstor.org/stable/4314732.

Haeberli, W., Vonder Mühll, D., 1996. On the characteristics and possible origins of ice in rock glacier permafrost. Zeitschrift für Geomorphologie N.F., 104, 43-57.

Haeberli, W., 1979. Holocene push-moraines in Alpine permafrost. Geografiska Annaler, 61A, 43-48. Doi: 10.2307/520513.

Hendrickx, H., Vivero, S., De Cock, L., De Wit, B., De Maeyer, P., Lambiel, C., Delaloye, R., Nyssen, J., Frankl, A., 2019. The reproducibility of SfM algorithms to produce detailed Digital Surface Models: an example of PhotoScan applied to a high-alpine rock glacier. Remote Sensing Letters, 10(1), 12-20. Doi: 10.1080/2150704X.2018.1519641.

Ikeda, A., Matsuoka, N., Kaab, A., 2008. Fast deformation of perennially frozen debris in a warm rock glacier in the Swiss Alps: An effect of liquid water. J. Geophys. Res., 113.

IPA – IPA Action Group Rock glacier inventories and kinematics, 2020. Baseline concepts towards standard guidelines for inventorying rock glaciers, v. 4.1, 1-12.

James, M.R., Chandler, J.H., Eltner, A., Fraser, C., Miller, P.E., Mills, J.P., Noble, T., Robson, S., Lane, S.N., 2019. Guidelines on the use of structure-from-motion photogrammetry in geomorphic research. Earth Surface Processes and Landforms, 44-10. https://doi.org/10.1002/esp.4637.

Kaufmann, V., Seier, G., Sulzer, W., Wecht, M., Liu, Q., Lauk, G., Maurer, M., 2018. Rock glacier monitoring using aerial photographs: conventional vs. UAV-based mapping – a comparative study. The International Archives of the Photogrammetry, Remote Sensing and Spatial Information Sciences, Volume XLII-1.

Kaufmann, V., Ladstädter, R., 2003. Quantitative analysis of rock glacier creep by means of digital photogrammetry using multi-temporal aerial photographs: two case studies in the Austrian Alps. In: Arenson,S. (Ed.), 8th International Conference on Permafrost.

Kellerer-Pirklbauer, A., Lieb, G.K., Kaufmann, V., 2017. The Dösen rock glacier in central Austria: a key site for multidisciplinary long-term rock glacier monitoring in the Eastern Alps. Austrian Journal of Earth Sciences, 110/2. Doi: 10.17738/ajes.2017.0013.

Kellerer-Pirklbauer, A., Kaufmann, V., 2012. About the relationship between rock glacier velocity and climate parameters in central Austria. Austrian Journal of Earth Sciences, 105/2, 94-112.

Kenner, R., Pruessner, L., Beutel, J., Limpach, P., Phillips, M., 2019. How rock glacier hydrology, deformation velocities and ground temperatures interact: examples from the Swiss Alps. Permafrost and Periglacial Processes, 31(1), 3-14. https://doi.org/10.1002/ppp.2023.

Kneisel, C., Kääb, A., 2007. Mountain permafrost dynamics within a recently exposed glacier forefield inferred by a combined geomorphological, geophysical and photogrammetrical approach. Earth Surface Processes and Landforms, 32(12), 1797-1810. Doi: 10.1002/esp.1488.

Kummert, M., Delaloye, R., 2018. Mapping and quantifying sediment transfer between the front of rapidly moving rock glaciers and torrential gullies. Geomorphology, 309, 60-76.

Lague, D., Brodu, N., Leroux, J., 2013. Accurate 3D comparison of complex topography with terrestrial laser scanner: application to the Rangitikei canyon (N-Z). ISPRS J. Photogramm. Remote Sens., 82, 10–26.

Loke, M.H., 2020. RES2DINV ver. 4.10 Rapid 2-D Resistivity and IP Inversion using the Least-Square Method, User Manual.

Lucieer, A., De Jong, S.M., Turner, D., 2014. Mapping landslide displacements using Structure from Motion (SfM) and image correlation of multi-temporal UAV photography. Progress in Physical Geography, 38(1), 97-116. Doi: 10.1177/0309133313515293.

Marcer, M., Serrano, C., Brenning, A., Bodin, X., Goetz, J., Schoeneich, P., 2019. Evaluating the destabilization susceptibility of active rock glaciers in the French Alps. The Cryosphere, 13, 141-155.

Mollaret, C., Hilbich, C., Pellet, C., Flores-Orozco, A., Delaloye, R., Hauck, C., 2019. Mountain permafrost degradation documented through a network of permanent electrical resistivity tomography sites. The Cryosphere, 13, 2557-2578. https://doi.org/10.5194/tc-13-2557-2019.

Muller, J., Vieli, A., Gärtner-Roer, I., 2016. Rock glaciers on the run – understanding rock glacier landform evolution and recent changes from numerical flow modelling. The Cryosphere, 10, 2865-2886. Doi: 10.5194/tc-10-2865-2016.

PermaNET, 2011. Guide lines for monitoring GST – Ground surface temperature. Permafrost Monitoring Network, V. 3 by P. Schoeneich.

PermaNET, 2011. Guide lines for monitoring BTS – Bottom temperature of snow cover. Permafrost Monitoring Network, V. 2 by P. Schoeneich.

PERMOS, 2019. Permafrost in Switzerland 2014/2015 to 2017/2018. Noetzli, J., Pellet, C., Staub, B. (Eds.), Glaciological Report (Permafrost), 16-19 of the Cryospheric Commission of the Swiss Academy of Sciences, 104 pp. Doi: 10.13093/permos-rep-2019-16-19.

PERMOS, 2016. Permafrost in Switzerland 2010/2011 to 2013/2014. Noetzli, J., Luethi, R., Staub, B. (Eds.), Glaciological Report (Permafrost), 12-15 of the Cryospheric Commission of the Swiss Academy of Sciences, 85 (2016).

Reynard, E., Delaloye, R., Baron, L., Chapellier, D., Devaud, G., Lambiel, C., Marescot, L., Monnet, R., 2003. Glacier/permafrost relationship in recently deglaciated forefields of small glaciers, Penninic Alps, Valais, Western Switzerland. Proceedings of the 8th International Conference on Permafrost, Zurich 2003, Vol. 1, 947-952.

Rossini, M., Di Mauro, B., Garzonio, R., Baccolo, G., Cavallini, G., Mattavelli, M., De Amicis, M. and Colombo, R., 2018. Rapid melting dynamics of an alpine glacier with repeated UAV photogrammetry. Geomorphology, 304, pp.159-172.

Staub, B., Lambiel, C., Delaloye, R., 2016. Rock glacier creep as a thermally-driven phenomenon: A decade of inter-annual observations from the Swiss Alps. XI International Conference on Permafrost, Postdam, Germany, 20-24 June 2016, 96-97.

Vivero, S., Lambiel, C., 2019. Monitoring the crisis of a rock glacier with repeated UAV surveys. Geogr. Helv., 74, 59-69. https://doi.org/10.5194/gh-74-59-2019.

Wahrhaftig, C., Cox, A., 1959. Rock glaciers in the Alaska Range. Bulletin of the Geological Society of America, 70(4), 383-436.

Westoby, M.J., Brasington, J., Glasser, N.F., Hambrey, M.J., Reynolds, J.M., 2012. «Structure-from-Motion» photogrammetry: a low-cost, effective tool for geosciences applications. Geomorphology, 179, 300-314. Doi: 10.1016/j.geomorph.2012.08.021.

Wigmore, O., Mark, B., 2017. Monitoring tropical debris-covered glacier dynamics from high-resolution unmanned aerial vehicle photogrammetry, Cordillera Blanca, Peru. The Cryosphere, 11, 2463-2480. https://doi.org/10.5194/tc-11-2463-2017.

Zahs, V., Hämmerle, M., Anders, K., Hecht, S., Sailer, R., Rutzinger, M.G., Williams. J., Höfle. B., 2019. Multi-temporal 3D point cloud-based quantification and analysis of geomorphological activity at an alpine rock glacier using airborne and terrestrial LiDAR. Permafrost and Periglac. Process., 30, 222-238. https://doi.org/10.1002/ppp.2004.